

Light-induced nonadiabatic photodissociation of the NaH molecule including electron-rotation coupling

Zoltán Király,¹ Otabek Umarov,² Csaba Fábri,¹ Gábor J. Halász,³ Attila Tóth,⁴ and Ágnes Vibók^{1,4}

¹*Department of Theoretical Physics, Doctoral School of Physics,
University of Debrecen, H-4002 Debrecen, PO Box 400, Hungary*

²*Department of Exact Sciences, Kimyo International University in Tashkent,
Shota Rustaveli Street 156, Tashkent 100121, Uzbekistan*

³*Department of Information Technology, University of Debrecen,
H-4002 Debrecen, PO Box 400 Hungary*

⁴*ELI ALPS, The Extreme Light Infrastructure ERIC,
Wolfgang Sandner str. 3, 6728 Szeged, Hungary*

Abstract

It is well established that electronic conical intersections (CIs) in molecular systems can be induced by laser light, even in diatomic molecules. The emergence of these light-induced degeneracies leads to strong coupling among electronic, vibrational, and photonic modes, which significantly influences ultrafast nuclear dynamics. In this work, we perform pump–probe numerical simulations on the NaH molecule, considering the first three singlet electronic states— ($X^1\Sigma^+(X)$, $A^1\Sigma^+(A)$ and $B^1\Pi(B)$) —and including several light-induced degeneracies in the theoretical model. To elucidate the ultrafast molecular dynamics, the combined effects of multiple light-induced nonadiabatic couplings and rotational motion of the nuclei together with the situation when the electronic angular momentum projected onto the diatomic axis couples with the angular momentum of the nuclei has been studied. We then calculate key dynamical observables such as dissociation probabilities, kinetic energy release spectra, and angular distributions of the photofragments within and above the linear regime.

I. INTRODUCTION

Understanding the behavior of atoms and molecules under strong electromagnetic fields has been an extensively investigated area of research. A large number of theoretical and experimental studies have been devoted to exploring a variety of novel phenomena arising from light–matter interactions. Many of these works focus on the dynamical behavior of diatomic systems, beginning with the simplest hydrogen-like ions or molecules and extending to systems containing a large number of electrons [1–5, 8–11, 13–16, 20–23, 29]. Nevertheless, numerous other important studies have also addressed the photodissociation and fragmentation of polyatomic molecules [34–43].

Molecular dissociation is commonly analyzed within the Born–Oppenheimer (BO) framework, which is based on the separation of electronic and nuclear motions due to their distinct time scales. In most cases, this approximation provides a satisfactory description of dynamical processes. However, at certain nuclear configurations—particularly in the vicinity of degeneracy points or conical intersections (CIs)—the energy exchange between electrons and nuclei becomes significant, leading to a breakdown of the BO approximation [44]. Conical intersections play a crucial role in nonadiabatic processes, serving as efficient funnels for ultrafast interstate transitions that typically occur on the femtosecond timescale [6, 45–49].

CIs in molecules can only form when a molecular system possesses at least two independent nuclear degrees of freedom. Consequently, since a diatomic molecule has only a single vibrational coordinate, CIs cannot arise in such systems under field-free conditions. However, this holds only in free space. When a diatomic molecule is exposed to a strong laser field, its electronic energy becomes dependent on the angle between the laser polarization direction and the molecular axis. This occurs because the interaction of the induced or permanent dipole moment with the external field generates an effective torque that tends to align the molecule with the field polarization.

Previous studies have demonstrated that laser waves can induce CIs even in diatomic molecules. In these cases, the rotational motion provides the additional degree of freedom required for the formation of a light-induced conical intersection (LICI) [50]. The presence of a LICI introduces strong nonadiabatic couplings through the mixing of rotational, vibrational, electronic and photonics modes. Importantly, the energetic and spatial locations of such LICIs can be controlled by tuning the laser field parameters, such as its intensity and frequency. Depending on the level of theoretical description, whether the rotational degree of freedom is accounted for as a parameter or a dynamic variable, the interaction with light can manifest as light-induced avoided crossing (LIAC) or LICI. In a restricted one-dimensional (1D) description, the molecular rotational angle is only a parameter

and thus can only mimic a light-induced avoided crossing situation (LIAC). However, in the full two-dimensional (2D) description, the rotational angle is a dynamic variable, the inclusion of which leads to a LICI explicitly included in the description. Numerous theoretical and experimental results in the past few years undoubtedly demonstrated that LICIs exert strong effects on the spectroscopic, quantum dynamical and topological properties of both diatomic [17–19, 25–27, 30–33, 51–62] and polyatomic systems [7, 12, 63–65], even for weak laser fields.

Recent publications [20–24, 28] pointed out that the coupling between the molecular rotational angular momentum (\mathbf{K}) and the total electronic angular momentum projected onto the molecular axis $\Omega = \Lambda + \Sigma$, i.e. \mathbf{K} - Ω coupling, might become important for the correct interpretation of rotation-related physical quantities. This effect is routinely neglected due to the large mass difference between molecules and electrons. However, at high laser intensities it can significantly alter the rotational degrees of freedom of molecules through repeated Rabi oscillations between the electronic states.

The goals of the present work are two-fold. First, efforts are made to find the appropriate pump and probe laser parameters (frequency, intensity, laser pulse length) that fall within or slightly above the linear regime. This makes analysis of the results easier. Second, we perform pump and probe numerical simulations to investigate the light-induced nonadiabatic photodissociation dynamics of the NaH molecule [29, 66–69] in the presence of nuclear as well as electron rotation. Next, in order to properly discuss the dissociation dynamics, the dissociation probabilities, kinetic energy release (KER) spectra, and photofragment angular distributions (PAD) are calculated. We perform 1D and 2D calculations to model the LIAC and LICI, respectively, as well as so-called 3D simulations, where beyond the nuclear rotational angular momentum we also incorporate the electronic interior angular momentum about the molecular-fixed z axis in our description.

The article is organized as follows. In the next section, we describe the methodology and algorithms employed in the theoretical analysis, including the working Hamiltonian, the applied electric fields, the computed dynamical quantities, and relevant numerical details. Section III presents and discusses the numerical results obtained for the NaH system. Finally, the main conclusions are summarized in the last section. Atomic units ($e = m_e = \hbar = 1$) are used throughout the paper, unless stated otherwise.

II. COMPUTATIONAL DETAILS

Our showcase example is the NaH molecule. As in case of our previous work [29] on the same system, our model includes the three lowest-lying singlet electronic states $X^1\Sigma^+$, $A^1\Sigma^+$ and $B^1\Pi$, la-

beled throughout the paper as X, A and B, respectively. $^1\Pi$ is a degenerate state. In the appendix we describe how it is used effectively as a single state in the calculations (Eq. A17). Their corresponding potential energy curves $V_{X/A/B}(R)$ are presented in Fig. 1 (a) along the $\vec{\mu}_{ii}(R) = \langle \phi_i | \sum_k \vec{r}_k | \phi_i \rangle$ permanent dipole moments (PDMs) on panel (b), and the $\vec{\mu}_{ij}(R) = \langle \phi_i | \sum_k \vec{r}_k | \phi_j \rangle$ transition dipole moments (TDMs) on panel (c), for $i, j \in \{X, A, B\}$. We note here that all permanent dipole moments of Σ states and $\Sigma - \Sigma$ TDMs are parallel, whereas those that involve the Π state are perpendicular to the molecular axis. Computation of the above electronic structure quantities of NaH has been carried out with the MOLPRO [70] program package at the MRCI/CAS(2/9)/aug-cc-pV5Z level of theory. The number of active electrons and molecular orbitals in the individual irreducible representations of the C_{2v} point group were $A_1 \rightarrow 2/5$, $B_1 \rightarrow 0/2$, $B_2 \rightarrow 0/2$, $A_2 \rightarrow 0/0$. Using these values we could achieve reasonable agreement with other results in the literature [71, 72].

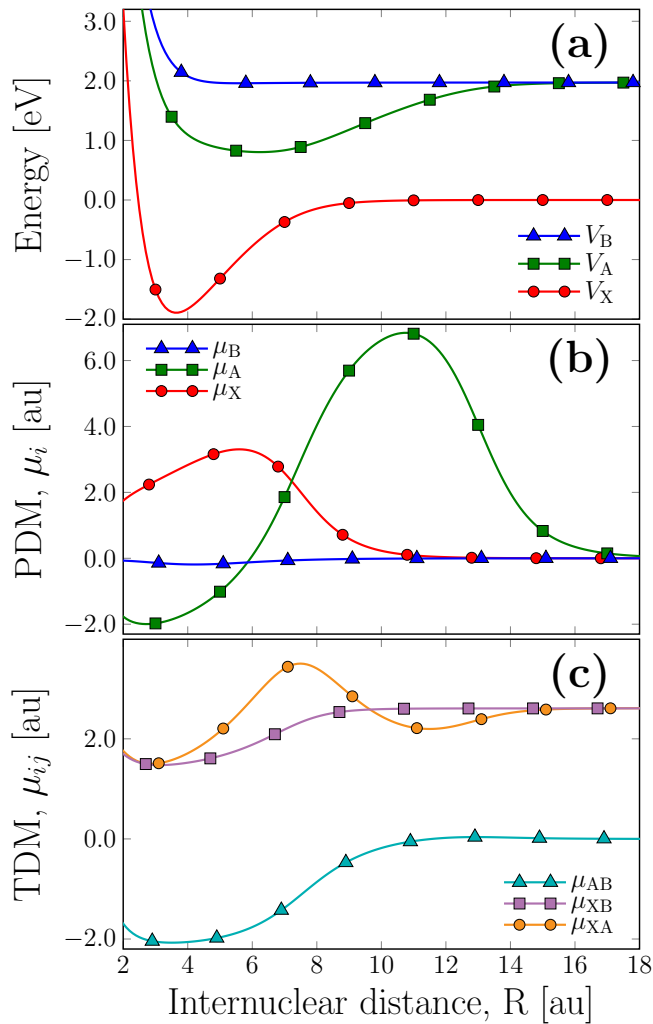


FIG. 1: (a) Lowest three adiabatic potential energy curves of the NaH molecule. (b) Permanent dipole moment (PDM) functions of the three adiabatic electronic states. (c) Transition dipole moment (TDM) functions between the different adiabatic electronic states.

A. The working Hamiltonian

As mentioned above, in the present work we extend our previously used model for light-matter interaction to include the \mathbf{K} - Ω coupling. A schematic representation of this scenario in Hund's case (a) is presented in Fig. 2. In this scheme, both the electronic orbital angular momentum \mathbf{L} and spin angular momentum \mathbf{S} are tied to the molecular axis with projections Λ and Σ on it. The total angular momentum \mathbf{J} of the system is the vector sum of this total interior angular momentum and the rotational angular momentum \mathbf{K} . Accordingly, the projection of \mathbf{J} onto the molecular axis, i.e. the body-fixed (BF) z axis, and the space-fixed (SF) Z axis are $\Omega = \Lambda + \Sigma$ and M , respectively.

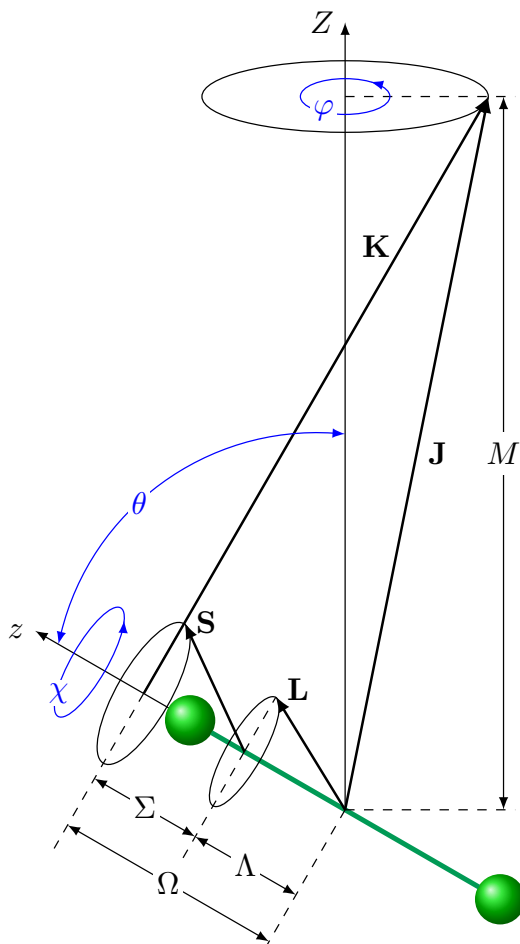


FIG. 2: Vector diagram of the electron-rotation coupling conforming to Hund's case (a). Λ and Σ are the projections of the electronic orbital \mathbf{L} and spin \mathbf{S} angular momenta onto the molecular axis, i.e. the z axis of the molecule-fixed (MF) frame. \mathbf{K} is the nuclear rotational angular momentum, and \mathbf{J} is the total angular momentum with M being its projection onto the space fixed (SF) Z axis. φ and χ are the Euler angles representing rotations around the SF Z and MF z axes, while θ is the angle between these two.

Molecular rotations are usually described in theoretical investigations in the basis of spherical harmonics or Legendre polynomials. However, this convention is unable to treat the \mathbf{K} - Ω coupling.

For this reason, the more general Wigner D basis

$$|JM\Omega\rangle = \sqrt{\frac{2J+1}{8\pi^2}} D_{M\Omega}^J(\varphi, \theta, \chi) = \sqrt{\frac{2J+1}{8\pi^2}} e^{-iM\varphi} d_{M\Omega}^J(\theta) e^{-i\Omega\chi} \quad (1)$$

is needed, where the Wigner D-functions $D_{M\Omega}^J(\varphi, \theta, \chi)$ are the matrix elements of the rotation operator $\mathbf{D}(\varphi, \theta, \chi)$. They may be represented as a product of three functions, each depending on a single argument, with $d_{M\Omega}^J(\theta)$ a real function known as the reduced Wigner D-function. The arguments φ and χ represent Euler angles of rotation around the SF Z and BF z axes, while θ is the Euler angle between these two axes, as presented in Fig. 2.

The time-dependent nuclear Hamiltonian of the NaH molecule in the space of the three lowest singlet electronic states interacting with a linearly polarized laser field $\mathcal{E}_Z(t)$ may be written as

$$\begin{aligned} \mathbf{H}(\mathbf{R}, t) = & \left(-\frac{1}{2M_r} \frac{\partial^2}{\partial R^2} + \frac{\mathbf{K}^2}{2M_r R^2} \right) \cdot \mathbf{1} + \begin{pmatrix} V_X(R) & 0 & 0 \\ 0 & V_A(R) & 0 \\ 0 & 0 & V_B(R) \end{pmatrix} - \\ & - \mathcal{E}_Z(t) \begin{pmatrix} \mu_{XX} \kappa_{XX} & \mu_{AX} \kappa_{AX} & \mu_{BX} \kappa_{BX} \\ \mu_{AX} \kappa_{AX}^\dagger & \mu_{AA} \kappa_{AA} & \mu_{BA} \kappa_{BA} \\ \mu_{BX} \kappa_{BX}^\dagger & \mu_{BA} \kappa_{BA}^\dagger & \mu_{BB} \kappa_{BB} \end{pmatrix}, \end{aligned} \quad (2)$$

where the first term describes the vibrational and rotational kinetic energy operator for the reduced mass M_r and internuclear distance R , and $\mathbf{1}$ is the three dimensional unit matrix. The second term stands for the potential energy operator with the potential energy curves $V_{X/A/B}(R)$ of the considered electronic states. The interaction term contains both the PDMs in the diagonal, and the TDMs in the off-diagonal elements, with

$$\kappa_{fi}(\theta, \chi) = \begin{cases} \cos \theta & \text{for } \Delta\Lambda_{f \leftarrow i} = 0 \\ -\sin \theta e^{\pm i\chi} & \text{for } \Delta\Lambda_{f \leftarrow i} = \pm 1. \end{cases} \quad (3)$$

Details of the derivation of this interaction term can be found in the Appendix A.

The working Hamiltonians used in our 1D and 2D calculations are obtained as a particular form of the above expression by setting $\Omega = 0$, and correspondingly $\chi = 0$. In this case the rotational angular momentum coincides with the total angular momentum of the system, $\mathbf{K} \equiv \mathbf{J}$, and the normalized Wigner D basis reduces the spherical harmonics, $|JM\Omega\rangle \rightarrow |JM\rangle \equiv Y_J^M(\theta, \varphi)$. Moreover,

the M -selection rule remains valid, so we recover our usual formalism [14, 15] in terms of the Legendre polynomials $P_J(\theta)$. Additionally, in the 1D model the rotational kinetic energy is completely neglected ($\mathbf{K}=0$) [53, 54].

B. The applied electric field

In the present work we investigated the photodissociation process of the NaH molecule in a pump-probe setup. Accordingly, the electric field \mathcal{E} entering the interaction term of our working Hamiltonian (2) is the sum of two linearly polarized pulses in the Z -direction

$$\mathcal{E}(t) \equiv \mathcal{E}_Z^{SF}(t) = \mathbf{e}_Z \mathcal{E}_{pm} f_{pm}(t) \cos(\omega_{pm}t) + \mathbf{e}_Z \mathcal{E}_{pr} f_{pr}(t) \cos(\omega_{pr}t), \quad (4)$$

with amplitudes \mathcal{E}_i and energy $\hbar\omega_i$. Both pulses were considered with cos-square-shaped envelope functions

$$f_i(t) = \cos^2\left(\frac{\pi(t-t_i)}{\tau_i}\right) \quad \text{for } i \in \{pm, pr\}, \quad (5)$$

where τ_{pm} and τ_{pr} are the durations of the pump and the probe pulse, respectively. The pump pulse, centered at $t_{pm} = 0$ fs (hence defining our time axis), initiates the dynamics of the system by transferring some part of the initial ground X state population to the first excited A state. The time delayed probe pulse, $t_{pr} = t_{pm} + \Delta t$ with $\Delta t = -25 \dots 1000$ fs, can either transfer population back from A to the X state or further promote to the dissociative B state.

As mentioned above, the position of light-induced conical intersections can be controlled by tuning the laser energy. In our previous study on the NaH molecule [29], the probe pulse was able to produce only a light induced avoided crossing between the X and A states. Here, we slightly increased its energy to $\hbar\omega_{pr} = 1.13$ eV which lead to two conical intersections ($\text{LICI}_1^{(XA)}$ and $\text{LICI}_2^{(XA)}$) between these surfaces, as can be seen on panel (a) of Fig. 3. The pump energy was set as the third-harmonic of this frequency, $\hbar\omega_{pm} = 3.39$ eV. For the pulse duration of the pump we chose $\tau_{pm} = 22$ fs, keeping its spectral width narrow enough to minimise population transfer to the B state. The probe pulse was $\tau_{pr} = 30$ fs long. With a pump intensity of $I_{pm} = 1 \times 10^{12}$ W/cm² we obtained meaningful excitation ($\sim 35\%$ on the A state) without Rabi floppings between X and A . In our numerical simulations we investigated two intensity regimes of the probe pulse. In the low intensity case of $I_{pr} = 1 \times 10^{11}$ W/cm² one-photon processes dominate, while for the higher intensity of $I_{pr} = 1 \times 10^{12}$ W/cm²

multiphoton processes may occur, and fingerprints of the electron-rotation coupling are expected to manifest.

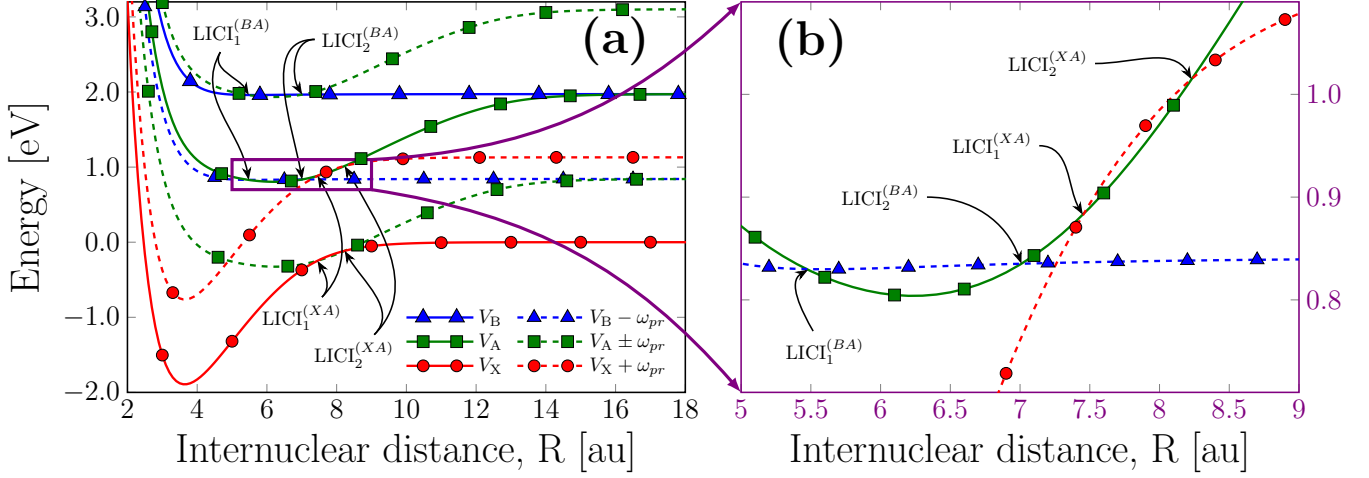


FIG. 3: (a) The three lowest-lying singlet adiabatic potential energy curves of the NaH molecule. The corresponding light-dressed states are denoted by dashed lines. The position of the light-induced conical intersections ($\text{LICI}_1^{(BA)}$, $\text{LICI}_2^{(BA)}$, $\text{LICI}_1^{(XA)}$ and $\text{LICI}_2^{(XA)}$) are also marked. (b) Magnification of the region highlighted on panel (a) with the light-induced conical intersections.

In order to illustrate the heart of the LICI concept, we employ the well-known Floquet framework (see [51–54] for a detailed discussion), which is commonly used to understand various phenomena in light-matter physics. The action of the probe pulse is described in this picture as the upward and downward shift of the potential energy curves by integer multiples of photon energy $n\hbar\omega_{pr}$. This is illustrated in Fig. 3 (panels (a) and (b)) for the most basic $n = 1$ one-photon case. As a result, the upward shifted first excited $V_A(R) + \hbar\omega_{pr}$ curve intersects the second excited $V_B(R)$ curve (or equivalently $V_A(R)$ is intersected by the downward shifted $V_B(R) - \hbar\omega_{pr}$), creating two light-induced conical intersections $\text{LICI}_1^{(BA)}$ and $\text{LICI}_2^{(BA)}$. The same phenomena appears for $V_A(R) - \hbar\omega_{pr}$ and $V_X(R)$ (identically between $V_X(R) + \hbar\omega_{pr}$ and $V_A(R)$) leading to $\text{LICI}_1^{(XA)}$ and $\text{LICI}_2^{(XA)}$. Diagonalizing the corresponding Floquet form of the Hamiltonian Eq. (2), one can obtain the light-induced adiabatic potential energy surfaces. The resulting conical intersections $\text{LICI}^{(fi)}$ between two states $i, f \in \{X, A, B\}$ appear in the configuration space whenever the conditions $V_i(R) \pm \hbar\omega_{pr} = V_f(R)$ (specifying its R -coordinate) and $\kappa_{fi}(\theta) = 0$ (see Eq. (3)) are simultaneously fulfilled. For parallel (i.e. $\Sigma \leftrightarrow \Sigma$ or $\Pi \leftrightarrow \Pi$) transitions this occurs at $\theta = \pi/2$, while for perpendicular ones ($\Sigma \leftrightarrow \Pi$) at $\theta = 0$ and $\theta = \pi$.

C. Nuclear wave packet propagation and calculated quantities

The nonadiabatic nuclear dynamics of the NaH molecule in the LIC1 framework was investigated by solving the time-dependent Schrödinger equation (TDSE) governed by the Hamiltonian of Eq. (2). Our simulations were performed with the multiconfigurational time-dependent Hartree (MCTDH) method implemented in the Heidelberg package [74–76]. The vibrational degree of freedom (R) was discretized by a Sin-DVR (sine discrete variable representation) with $N_R = 512$ grid points distributed in the internuclear coordinate range [2.0, 50.0] au. The rotational degree of freedom (θ) was expanded in the basis of Legendre polynomials for the conventional description, and in the basis of L_2 normalized Wigner D-functions when the \mathbf{K} - Ω electron-rotation coupling was included. In both cases $N_\theta = 91$ basis functions were employed. The Wigner D basis was further constructed with $N_\chi = 11$ and $N_\varphi = 1$ exp-DVR functions for χ and φ , respectively. In the MCTDH formalism, these so called primitive basis sets (η) are used to represent the single particle functions (SPF)

$$\phi_{j_q}^{(q)}(q, t) = \begin{cases} \sum_{l=1}^{N_q} c_{j_q l}^{(q)}(t) \eta_l^{(q)}(q), & q \in \{R, \theta\}, \\ \sum_{l_\theta=1}^{N_\theta} \sum_{l_\varphi=1}^{N_\varphi} \sum_{l_\chi=1}^{N_\chi} c_{j_q l_\theta l_\varphi l_\chi}^{(q)}(t) \prod_{f \in \{\theta, \varphi, \chi\}} \eta_{l_f}^{(f)}(f), & q = (\theta, \varphi, \chi). \end{cases} \quad (6)$$

The second expression applies in the \mathbf{K} - Ω case, when the primitive basis functions of the θ , φ and χ degrees of freedom are combined into a single MCTDH mode to form three-dimensional single-particle functions. The SPFs are used in turn to build up the wave function

$$\psi(R, \rho, t) = \sum_{j_R}^{n_R} \sum_{j_\rho}^{n_\rho} A_{j_R j_\rho}(t) \phi_{j_R}^{(R)}(R, t) \phi_{j_\rho}^{(\rho)}(\rho, t), \quad \text{where } \rho \in \{\theta, (\theta, \varphi, \chi)\}. \quad (7)$$

Throughout our simulations, the single-particle basis size was $n_R = n_\rho = 20$ for both modes in the expansion of the wave function, which ensured the convergence of the results.

A complex absorbing potential (CAP) of the form $-iW(R) = -i\eta(R - R_c)^3\Theta(R - R_c)$ is applied to the vibrational degree of freedom on all three surfaces in order to keep the length of its primitive grid manageable while preventing spurious reflections. The starting point and strength of the CAP were $R_c = 40$ [au] and $\eta = 1.2 \times 10^{-5}$, respectively, while the Heaviside's Θ function means that it affects the $R > R_c$ region. It was also used to perform flux analysis [76] to obtain physical quantities of the photodissociation process such as the kinetic energy release spectra (KER) or the photofragment

angular distribution (PAD)

$$P_{\text{KER}}(E) = \int_0^\infty dt \int_0^\infty dt' \langle \psi(t) | W | \psi(t') \rangle e^{-iE(t-t')}, \quad (8)$$

$$P_{\text{PAD}}(\theta_j) = \frac{1}{w_j} \int_0^\infty dt \langle \psi(t) | W_{\theta_j} | \psi(t) \rangle. \quad (9)$$

In the above expression of the PAD, θ_j and w_j are the specific angles and their corresponding quadrature weights in the applied DVR, while $-iW_{\theta_j}$ is the projection of the CAP onto these grid points. Strictly speaking, the angular distribution of Eq. (9) gives the probability of photodissociation in the solid angle $(\Omega, \Omega + d\Omega)$ in the direction (θ, φ) . Due to the cylindrical symmetry of the problem, also exploited when choosing a Legendre basis instead of spherical harmonics for the rotational degree of freedom in our 1D and 2D models, it is independent of φ . Alternatively, we may calculate the total photofragment angular distribution in the θ_j direction by integrating Eq. (9) along φ as

$$\tilde{P}_{\text{PAD}}(\theta_j) = \int_0^{2\pi} P_{\text{PAD}}(\theta_j, (\varphi)) \sin \theta_j d\varphi \propto \int_0^\infty dt \langle \psi(t) | W_{\theta_j} | \psi(t) \rangle, \quad (10)$$

where in the final expression we used the fact that the quadrature weights are proportional to $\sin \theta_j$.

The total dissociation probability is easily obtained by integrating either of the above quantities

$$P_{\text{diss}} = \int_0^\infty P_{\text{KER}}(E) dE = \int_0^\pi P_{\text{PAD}}(\theta) \sin \theta d\theta = 2 \int_0^\infty dt \langle \psi(t) | W | \psi(t) \rangle. \quad (11)$$

To demonstrate the impact of light-induced nonadiabatic effects on the dissociation dynamics of NaH we compare results obtained with two levels of theory relative to the rotational degree of freedom θ . In the full two-dimensional (2D) case θ is considered as a dynamical variable, while in the restricted one-dimensional (1D) situation it is only a parameter. This means that the original orientation of the molecules remain unchanged during the evolution of the system, and they experience an effective field strength $\mathcal{E}^{eff}(\theta) = \mathcal{E}_{pm,pr} \kappa_{fi}(\theta)$, corresponding to the effective intensity $I_0^{eff}(\theta) = I_0 \cos^2 \theta$ or $I_0^{eff}(\theta) = I_0 \sin^2 \theta$, through the permanent and transition dipoles depending on the symmetry of the involved electronic states. The difference of the two descriptions is that the degeneracy points between the potential energy surfaces manifest as LICIs in 2D and LIACs in 1D. Our third type of simulations, referred as 3D, explore the impact of electron-rotation coupling in the LICl picture.

III. RESULTS AND DISCUSSION

The aim of this work is to describe and characterize the photodissociation dynamics of a non-aligned, isotropically distributed NaH molecule in the presence of light-induced conical intersections, and to explore the effect of the usually neglected electron-rotation coupling on this process. To this end, we compute dissociation probabilities, kinetic energy release (KER) spectra, and photofragment angular distributions (PAD) in a pump-probe setup.

The system is assumed to be initially prepared in its electronic (X), vibrational ($\nu = 0$), and rotational ($J = 0$) ground state. The dynamics is initiated by the pump-pulse, which promotes about 35% of the population to the A state. The excited wave packet starts to oscillate within an interval of $R \approx 3 - 12$ a.u.. This field-free (without a probe pulse) time evolution is displayed in Fig. 4 a). A reasonably good indicator for the instantaneous position of the wave packet is the expectation value of the internuclear distance $\langle \psi(t) | R | \psi(t) \rangle$. This quantity is overlaid on top of the vibrational density map (integrated over the angular degrees of freedom) of Fig. 4 a) with a continuous magenta curve. During the initial stages, within the first period of the vibrational motion, the wavepacket is well localized, and the R -expectation value follows it almost exactly. As time progresses, due to the multiple vibrational components with different energies (and periods), the wavepacket becomes increasingly more diffuse, therefore the R -expectation curve is only able to reflect the overall periodicity of the motion.

The horizontal lines in Fig. 4 indicate the internuclear distances where light induced conical intersections are formed by the probe pulse, as in Fig. 3. Specifically, the continuous and the dotted lines at $R = 5.48$ [a.u.] and $R = 7.01$ [a.u.] indicate the intersections of the $V_B(R)$ and $V_A(R)$ potential energy curves, that is $\text{LICI}_{1,2}^{(BA)}$. Similarly, the dashed and dash-dotted lines mark the $\text{LICI}_{1,2}^{(XA)}$ positions at $R = 7.45$ [a.u.] and $R = 8.23$ [a.u.] between the $V_X(R)$ and $V_A(R)$ curves. Dissociation in the individual electronic channels is expected to take place around those probe delay times when the vibrational wavepacket traverses the interaction regions. These are marked for the dissociative B state with blue circles and blue plus signs for $\text{LICI}_1^{(BA)}$ and $\text{LICI}_2^{(BA)}$, respectively. For later times the R -expectation curve does not reach the $\text{LICI}_1^{(BA)}$ distance, but the wavepacket clearly does. For population with sufficiently high kinetic energy dissociation can occur on state X at $\text{LICI}_1^{(XA)}$ and $\text{LICI}_2^{(XA)}$ marked with red squares and red \times signs, respectively.

Panels b) and c) of Fig. 4 highlight the two time windows of the above dynamics we focus on in the rest of this work. Here, the R -expectation value and the LICI indicators (horizontal lines and markers) are reproduced on the left y -axis. The data belonging to the right y -axis shows the time

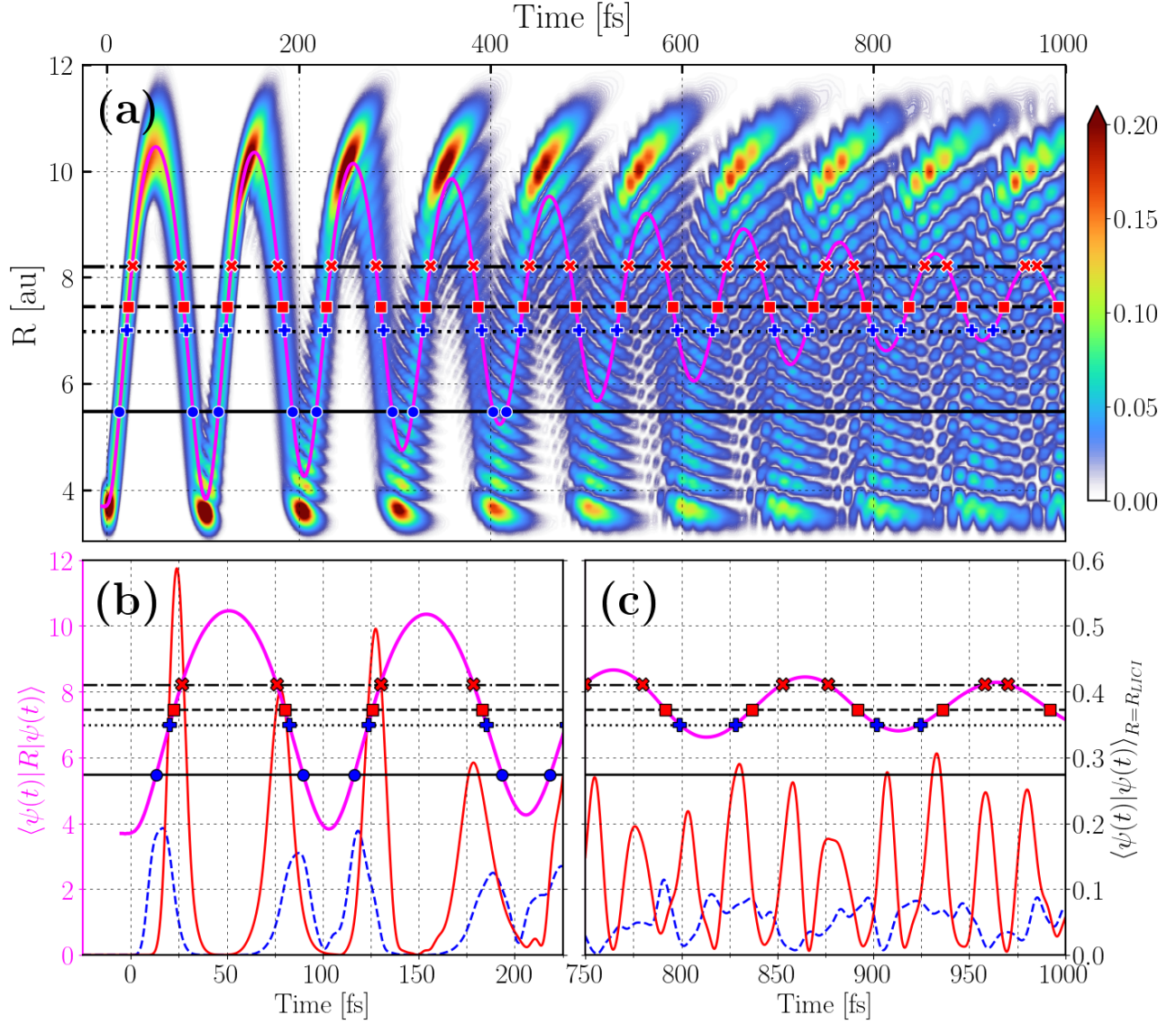


FIG. 4: (a) Vibrational motion of the nuclear wave packet on the A state after excitation by the pump pulse, and the expectation value of the R coordinate (magenta curve). The horizontal lines show the LICI positions, while the markers indicate when the R -expectation curve crosses them: $\text{LICI}_1^{(BA)}$ continuous line / blue circles; $\text{LICI}_2^{(BA)}$ dotted line / blue plus signs; $\text{LICI}_1^{(XA)}$ dashed line / red squares; and $\text{LICI}_2^{(XA)}$ dash-dotted line / red \times signs. Panels (b) and (c) zoom in the two investigated delay time windows, and show the R -expectation curve and LICI position indicators as on panel (a), along the TDM weighted sums of the nuclear wavepacket density at $\text{LICI}_{1+2}^{(BA)}$ with dashed blue line, and $\text{LICI}_{1+2}^{(XA)}$ with continuous red line.

evolution of the nuclear wavepacket density at the crossings to state B with dashed blue line and X with continuous red line. To be more exact, the vibrational densities at the internuclear distances ($R_{\text{LICI}_1^{(fA)}}$ and $R_{\text{LICI}_2^{(fA)}}$) corresponding to crossings between the same two potential energy curves are weighted with the appropriate transition dipole values and summed together. This quantity may serve as a crude indicator of the dissociation yield in the corresponding channels.

A. Total Dissociation probability

The total dissociation yields on the individual electronic states (X: red, circle; A: green, square; B: blue, triangle) calculated with Eq. (11) within the 1D (dashed), 2D (continuous) and 3D (dotted) models are presented in Fig. 5. The upper row (panels a) and b)) show the results obtained in the two delay-time windows for $I_{pr} = 1 \times 10^{11}$ W/cm², while the lower row (c) and d)) for the higher employed pump intensity $I_{pr} = 1 \times 10^{12}$ W/cm². In case of the low I_{pr} the probability curves corresponding to the B and X states mimic nicely the density curves presented in Fig. 4 b) and c). This indicates that one-photon transition is the dominant mechanism, and in this range the dissociation yields scale linearly with the intensity. In the small Δt window the dissociation probabilities show well separated peaks which align perfectly with the transition times defined by the intersection of the R -expectation curve and the LIC1 lines. For large delay times we do not get such well defined structures due to the blurring of the excited wavepacket. For the higher intensity the result for state B roughly double in value, which shows that we are still in the linear regime, but the peaks are distorted due to saturation. In contrast, dissociation probability in the A channel does not increase, instead certain peaks even get diminished. This is explained by the fact that the vibrational wavepacket encounters the B crossings first, and as a result by the time it reaches LIC1_{1,2}^(XA) there is less population available for transition. For large Δt values the dissociation yield curves become more structured, which reflects the interference pattern of the different wave packet vibrational components seen in the density map of Fig. 4 a). Figure 5 contains a third group of data, shown with green lines with squares. These represent dissociation on the A state. This is inherently a two-photon process, population transfer from A to B and/or X followed by transfer back to A, which has a lower probability. For this reason it has to be scaled up to be visible on the same scale as the other two dissociation probabilities. The ratio of the scaling factors, $f_{sc}=3000$ for the low and $f_{sc}=30$ for the high intensity, and the approximate doubling of its value for an order of magnitude increase of the intensity confirms this mechanism.

Comparing the results obtained with the three approaches, we see that for small delay times they essentially coincide. For large Δt the 2D and 3D data remain indistinguishable, but the 1D curves deviate noticeably. In the X channel it consistently lie below the 2D/3D curves, while in the B channel it yields higher dissociation values for all delay times. This is true for both employed probe intensities. These observations are jointly determined by molecular rotation and the emerging light-induced nonadiabatic effects. The pump pulse initiates the rotational motion of the molecule. However, this is a relatively slow process and its influence is not yet apparent at short delay times.

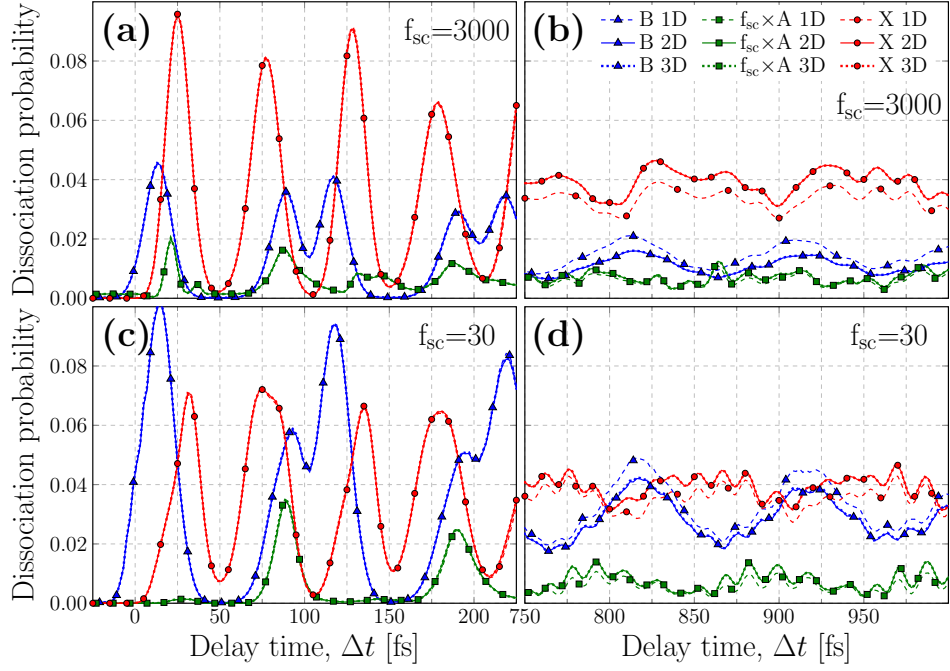


FIG. 5: Dissociation probabilities corresponding to the individual adiabatic electronic states (X - red with circles, A - green with squares, B - blue with triangles) as a function of delay time between the pump and the probe pulses. The A state dissociation probability is scaled for better visibility, with the scaling factor f_{sc} indicated on each panel. The dashed, continuous and dotted lines correspond to results obtained with the 1D, 2D and 3D models, respectively. Panels (a) and (b) show our results for $I_{pr} = 1 \times 10^{11}$ W/cm², while (c) and (d) for $I_{pr} = 1 \times 10^{12}$ W/cm²

As a consequence, in this domain, the dissociation probabilities calculated with the three models are identical. For later times, the rotation manifests in the alignment of the molecules along the laser polarization, i.e. Z -axis. This means, when the probe pulse arrives, it interacts with more favorably oriented molecules than in the 1D approach, where rotation is neglected. Due to the symmetries of the electronic states, this alignment enhances the coupling between the $A \leftrightarrow X$ states and reduces the one between $A \leftrightarrow B$. This explains the trends observed between the results obtained with the models that include rotational motion (2D, 3D) and the 1D that neglects it. For this physical quantity, the incorporation of electron-rotation in the description does not show any effect.

B. Kinetic Energy Release Spectra

To illustrate the time-delay dependence of the kinetic energy release spectra of the photofragments, we present in Fig. 6 the results obtained with the 2D model at the higher investigated intensity. Panels in different rows correspond to spectra of the individual electronic states. At short delay times, shown in left column, the spectra exhibit well defined peaks around the time moments the

excited wave packet on the A state crosses one of the LICs. In contrast, for long delay times as the different vibrational components of the excited wave packet do not reach the coupling regions simultaneously, more elongated and structured features emerge.

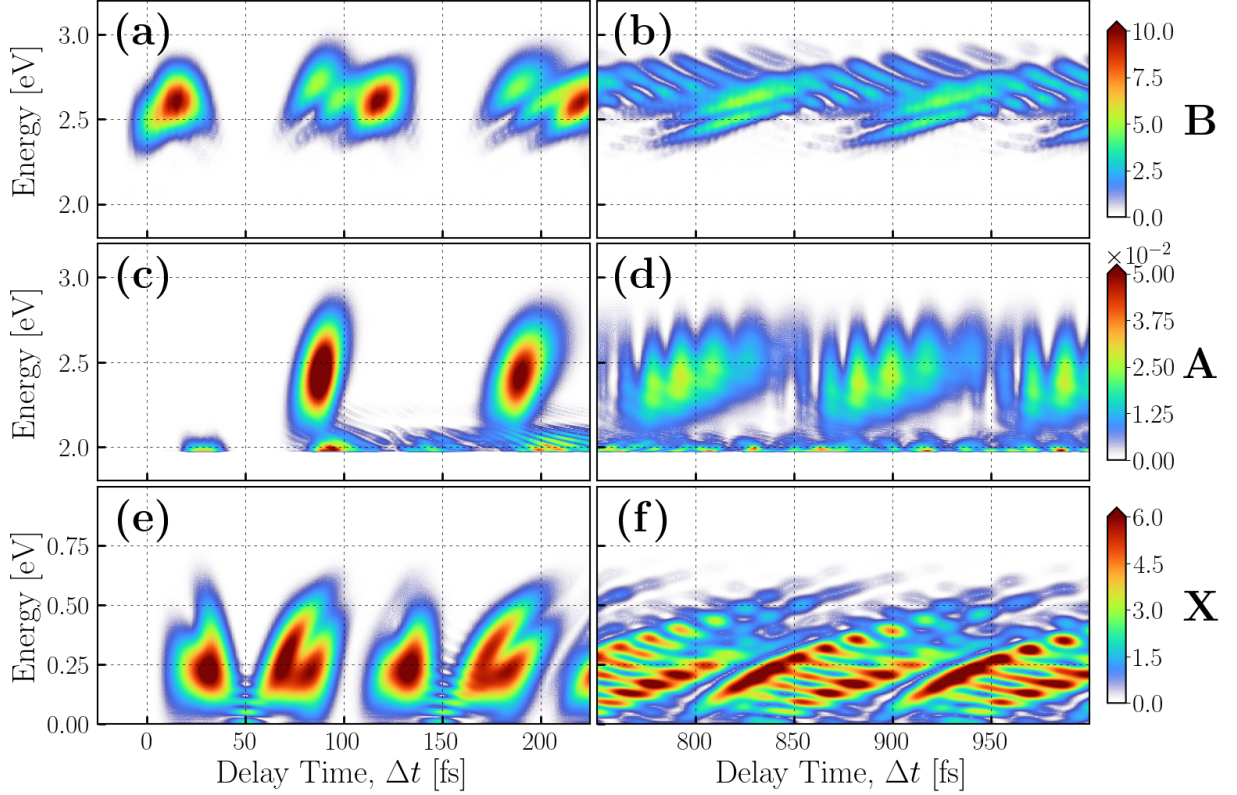


FIG. 6: Kinetic energy release (KER) spectra of the photofragments for $I_{pr} = 1 \times 10^{12}$ W/cm² as a function of delay time for the 2D model on each dissociation channel: B state (a, b); A state (c, d); X state (e, f).

From our previous work [29] it is already known, that the 1D and 2D models yield nearly identical KER spectra at short delay times. At longer delays, however, significant differences emerge due to the combined effect of the rotational motion initiated by the pump pulse and the light-induced nonadiabatic dynamics. These mechanisms have been discussed above describing the differences observed in the dissociation yields calculated with the different methods.

The primary focus of the present study is to highlight possible effects of the electron-rotation coupling that the simpler models might neglect. For this reason, we present in Fig. 7 the relative difference between the 2D and 3D KER spectra on the X and B states for both investigated probe-pulse intensities. The spectra on the A state is orders of magnitude smaller than on the other two channels, as indicated by the scale of the colorbars of Fig. 6, therefore they are omitted. It can be seen that the differences are more pronounced on the B state. This is not surprising, since the \mathbf{K} - Ω coupling affects transitions involving this state directly. Also, with increased intensity the differences

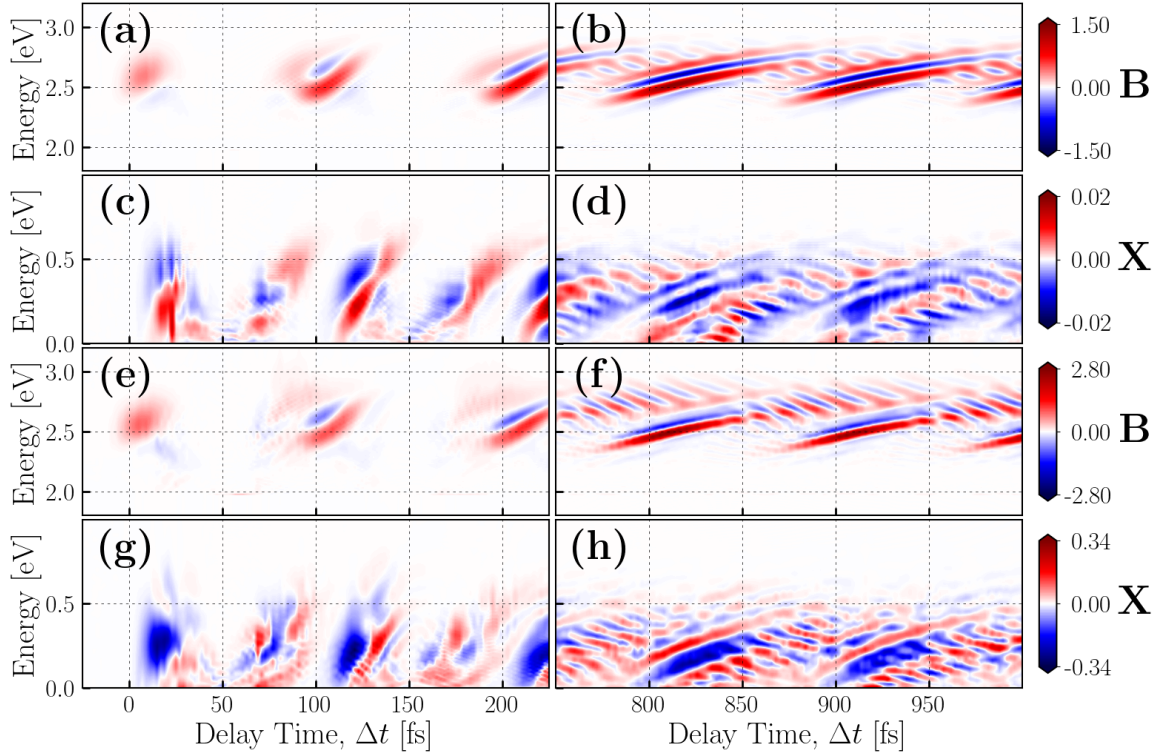


FIG. 7: Relative difference between the KER results obtained in the 2D and 3D models for the B and X dissociation channels. The color scale represents percentages. Panels (a)-(d) show the results for $I_{pr} = 1 \times 10^{11}$ W/cm², while (e)-(h) for $I_{pr} = 1 \times 10^{12}$ W/cm², respectively.

intensify, but do not exceed 2-3% even for the higher employed intensity (Fig. 7 panels e) and f)). We may conclude that, in agreement with the results obtained for the dissociation yield, the inclusion of electron-rotation coupling does not alter the KER spectra in a measurably meaningful way.

C. Photofragment Angular Distribution

Let us turn our attention to the angular distribution of the photofragments. Within the short delay time interval, as we saw earlier for the other quantities, the PAD (Eq. 9) calculated with the three employed models produce identical results. Therefore, the corresponding data is not presented here. Likewise, the results obtained for the two intensities display the same trends. Accordingly, we show in Fig. 8 only the high intensity results for each electronic state and for the 1D, 2D and 3D models.

Two observations stand out at first glance: i) The angular distributions on the Σ states (X and A) obtained with the 2D and 3D models are essentially indistinguishable. In contrast, within the 1D approximation – where molecular rotation is completely neglected – the results differ significantly

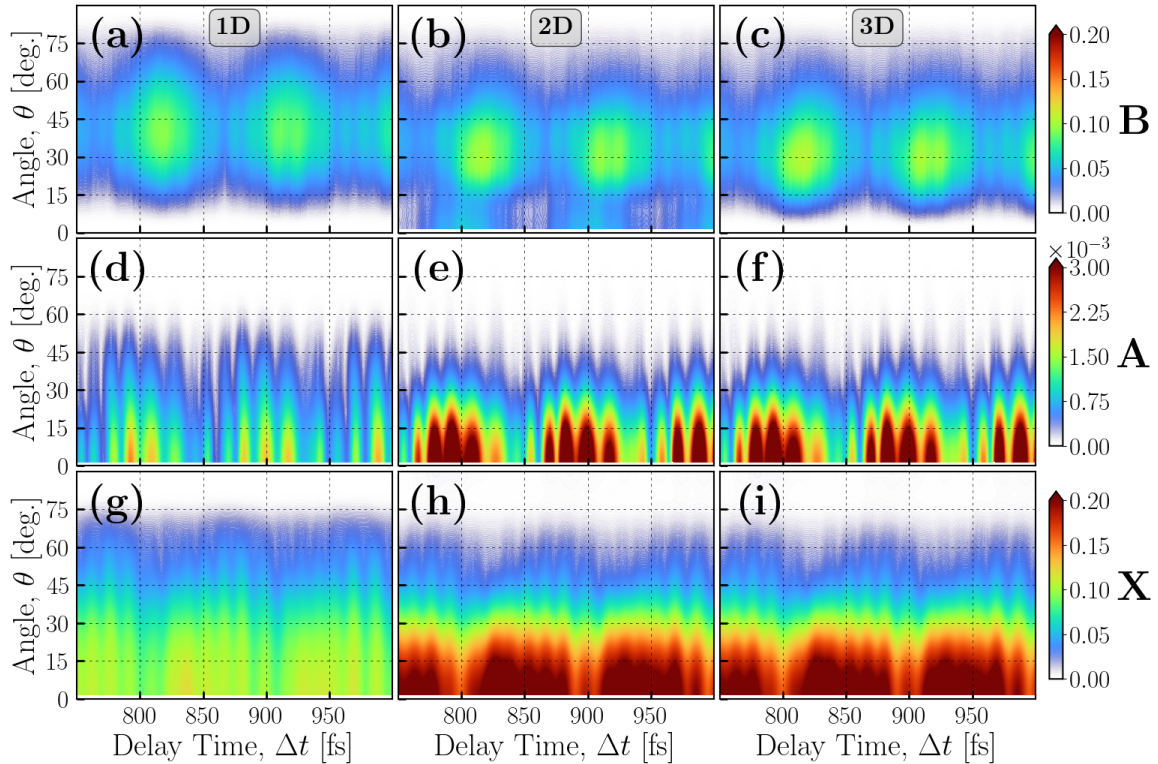


FIG. 8: Photofragment angular distribution (PAD) conform Eq. (9) as a function of delay time for $I_{pr} = 1 \times 10^{12}$ W/cm² on each dissociation channel: B state (a)-(c); A state (d)-(f); X state (g)-(h). Different columns correspond to the 1D, 2D and 3D model calculations, as indicated on the upper row.

from the others. The underlying mechanism is essentially the same as identified earlier for the interpretation of the dissociation yields. To be specific, due to the rotational motion induced by the pump pulse, the pump excited molecules start to deviate from their initial isotropic distribution and align with the polarization direction of the employed laser fields. The same symmetry of the X and A states means their coupling is proportional to $\cos \theta$, i.e. strongest along the polarization direction. As a result, a larger portion of the population transfers back and dissociates on the X state than in the rotationless 1D situation. The distinctive substructure of elongated vertical peaks is a direct consequence of the different vibrational components of the wave packet reaching the coupling region at different times.

ii) The results for the B state obtained with the 2D and 3D models differ markedly in the small-angle region ($\theta \approx 0^\circ - 15^\circ$). This is a clear fingerprint of the inclusion of electron-rotation coupling into the description. Similar findings were reported by the group of S. B Zhang, when studying the photofragment angular distribution of the the CH⁺ and MgH⁺ molecules [22, 24]. Another noteworthy observation – one that has not been examined previously – is that the PAD data obtained with the 3D method converges to the 1D results for small angles.

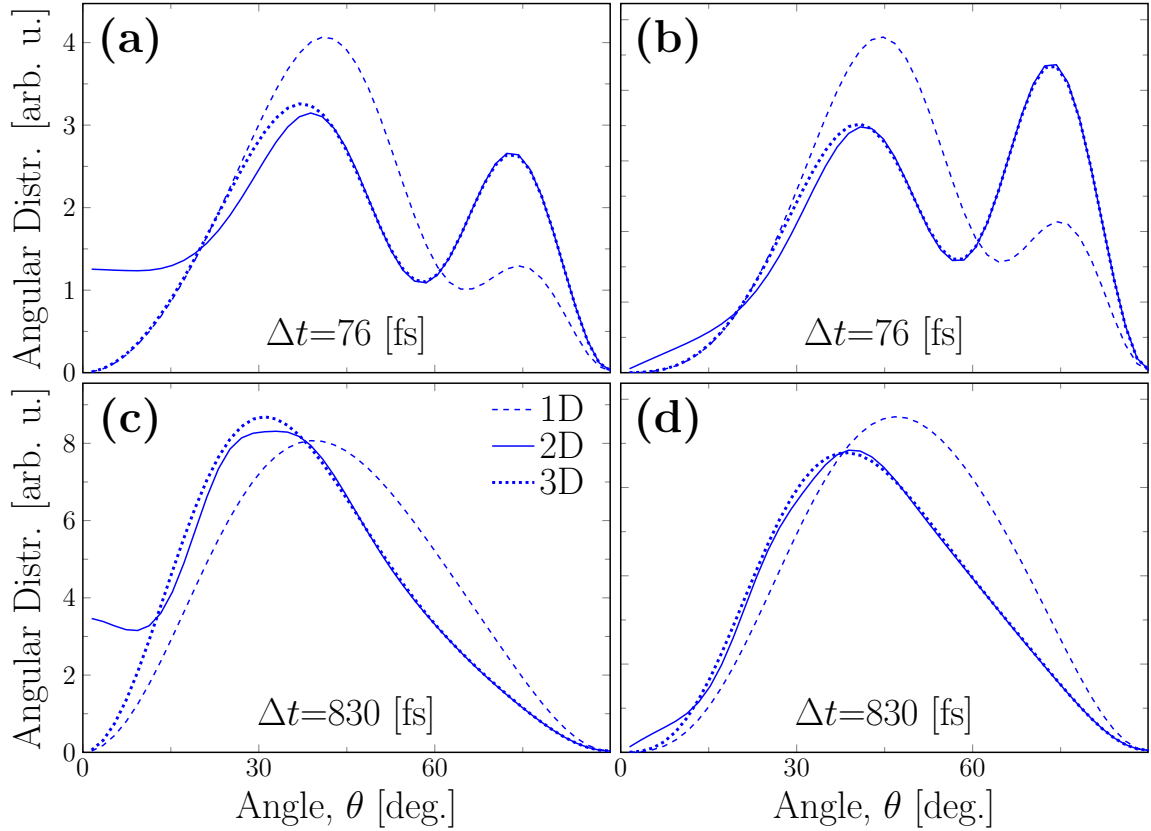


FIG. 9: Angular distribution on the B state for two delay times indicated on the figures. Panels (a) and (c) show the results calculated with Eq. (9), while (b) and (d) with Eq. (10). Dashed, continuous and dotted lines represent the 1D, 2D and 3D models, respectively.

For easier visualization, panels a) and c) of Fig. 9 present the angular distributions calculated with Eq. (9) within the three models for two specific delay times and for the higher probe intensity. As mentioned above, the $\Sigma \leftrightarrow \Sigma$ transitions are proportional to $\cos\theta$, and with the chosen pump intensity (no Rabi floppings) the pump-excited wave packet on A has a “ p_z ”-shape (dominantly $J = 1$). On the other hand, $\Pi \leftarrow \Sigma$ transitions are proportional to $\sin\theta$. The combined effect leads in the rotationally static 1D model on the B state to a vanishing PAD both at $\theta = 0^\circ$ and 90° , and a maxima around $\theta \sim 40^\circ$. When molecular rotation is switched on (2D, 3D), the molecules tend to align along the laser field, and the p_z shape of the A wavepacket is skewed toward the Z -axis. This induces a shift of the B state PAD toward smaller angles. Moreover, the light induced conical intersections between the A and B states appear at $\theta = 0^\circ$ (and 180°), which facilitates dissociation on B around, the otherwise forbidden, $\theta = 0^\circ$ angles. As our data shows, incorporating also the $\mathbf{K}\text{-}\Omega$ coupling in the description entirely suppresses this effect, leading to no dissociating fragments along the Z -axis. For increasing laser intensity the coupling becomes stronger, i.e. steeper adiabatic surfaces that guide the wave packet more efficiently toward the LICI in 2D, and the discrepancy with

the 3D model becomes ever higher [24].

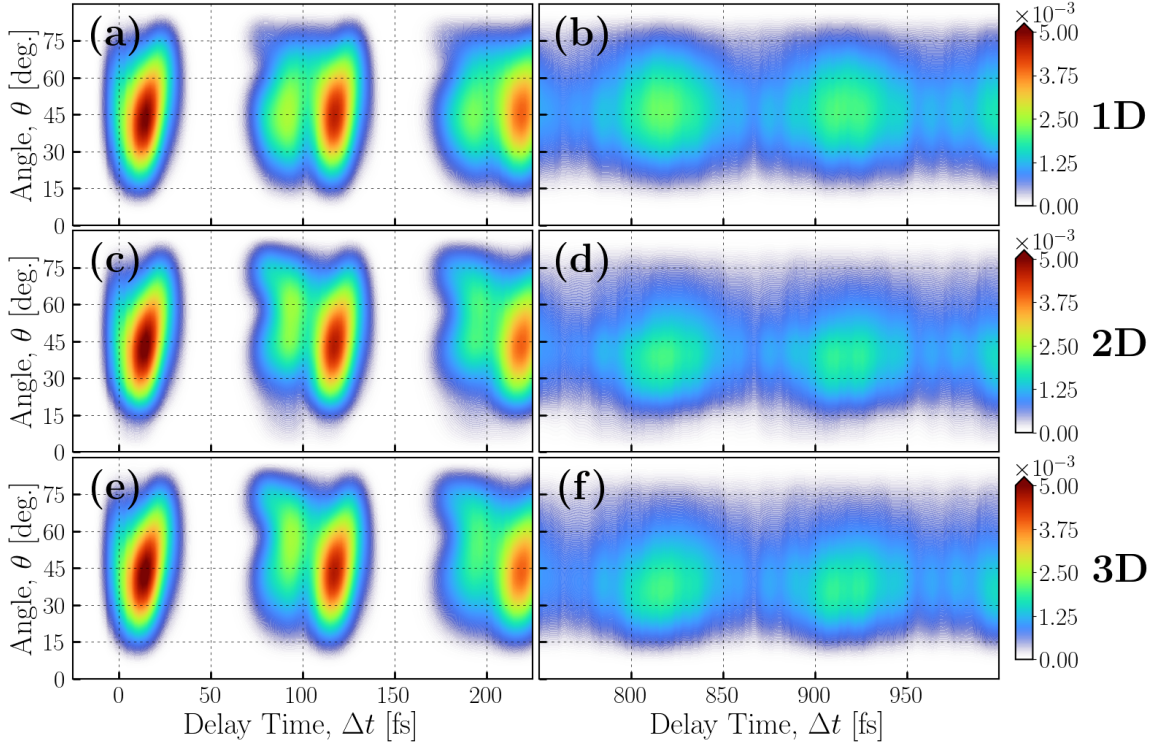


FIG. 10: Total angular distribution along θ on the B state for $I_{pr} = 1 \times 10^{12}$ W/cm² conform Eq. (10).

Let us recall that in the dissociation probability and KER spectra we did not see significant differences between the 2D and 3D results. To better understand this discrepancy, we also calculated the total photofragment angular distributions $\tilde{P}_{PAD}(\theta)$ along the polar angle θ according to Eq. (10). The results are presented in Fig. 10 and panels (b) and (d) of Fig. 9. We can see, that the integration over the azimuthal angle φ essentially washes out the differences between the two descriptions. This is not surprising, since the integration is equivalent (up to a constant factor) with a multiplication with the quadrature weights (i.e. $\sin \theta$), which diminishes the differences most strongly in the vicinity of $\theta = 0^\circ$, where they are the largest.

IV. CONCLUSIONS

In the present paper we performed pump-probe numerical simulations to study the ultrafast molecular dynamics of the NaH molecule, considering its first three singlet electronic states. To elucidate the underlying mechanisms, we have investigated the combined effects of multiple light-induced nonadiabatic couplings and nuclear rotational motion, including the case where the electronic angular momentum projected onto the diatomic axis is coupled to the rotational angular momentum

of the nuclei. For this reason key dynamical observables —namely dissociation probabilities, kinetic energy release spectra, and photofragment angular distributions— for intensities at the upper end of the linear regime have been computed.

Based on our results, we can conclude that for dissociation probabilities and kinetic energy release spectra, the difference between the 1D and 2D methods is much more pronounced than that between the 2D and 3D approaches. This is understandable, since the 2D model explicitly includes nuclear rotation and the associated light-induced nonadiabatic effects, which are absent in the 1D treatment. In contrast, the discrepancies between the 2D and 3D methods are comparatively minor for these observables.

However, in the case of angular distributions, we observed a substantial difference between the 2D and 3D results in the small θ angle region. These discrepancies intensify with increasing laser intensities. Interestingly, the 3D model yields results that are closer to those obtained with the more restrictive 1D model. Presently, the underlying mechanism of this behavior is not clear, and will be the subject of further investigations.

To gain a more accurate understanding of this behavior, we recalculated the dissociation probabilities along the θ direction. With this integration along the azimuthal angle φ , the 2D and 3D models produce similar results even in the small-angle region. This does not imply that electron–rotation coupling has no effect; rather, it suggests that its impact should not be overestimated, at least for the considered laser intensities.

Acknowledgments

The authors are indebted to NKFIH for funding (Grant No. K146096). The ELI ALPS project (GINOP-2.3.6-15-2015-00001) is supported by the European Union and co-financed by the European Regional Development Fund. This paper was supported by the János Bolyai Research Scholarship of the Hungarian Academy of Sciences.

V. DATA AVAILABILITY

The data that support the findings of this article are openly available [\[77\]](#); embargo periods may apply.

Appendix A: Laser-matter interaction in Wigner D basis

The operator of light-matter interaction in the dipole approximation is the scalar product between the $\mathcal{E}(t)$ electric field and the dipole operator $\boldsymbol{\mu}$ (permanent or transition). The electric field defines the space-fixed (SF) Cartesian coordinate system, where in case of a linearly polarized laser, for convenience, the polarization axis coincides with the SF Z -axis. Dipole moments are supplied by quantum chemistry packages, and are defined in body-fixed (BF) Cartesian coordinates, but can be transformed to SF with the help of the rotation operator as:

$$\boldsymbol{\mu}^{SF} = \mathbf{D}(\varphi, \theta, \chi) \boldsymbol{\mu}^{BF} \quad (\text{A1})$$

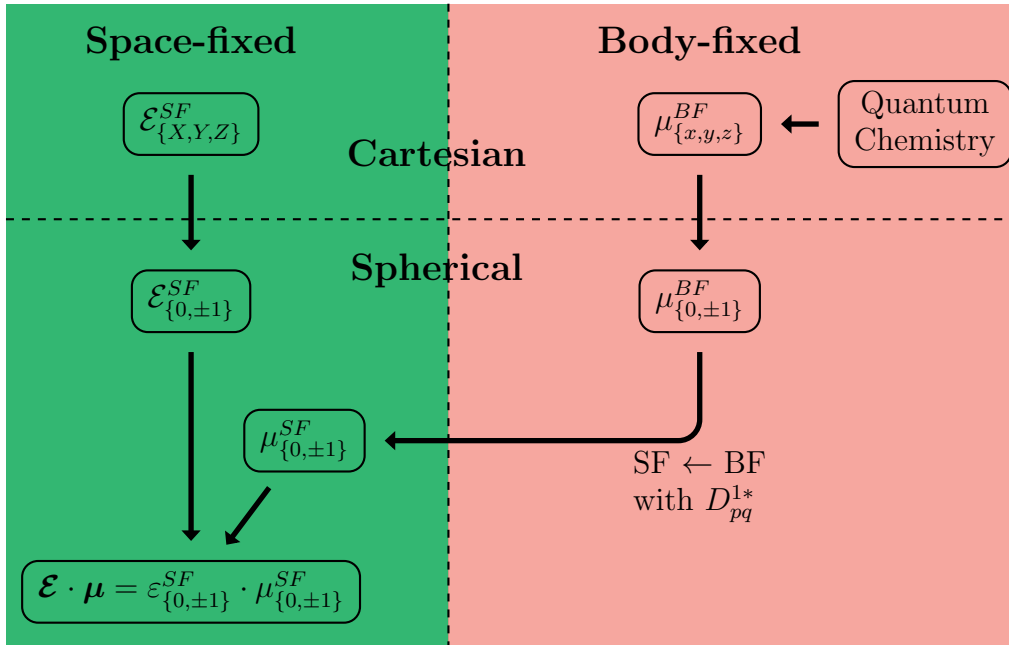


FIG. 11: Workflow for the development of laser-matter interaction.

This expression is best cast in spherical coordinates, where vectors are written as

$$\mathbf{v} = \sum_q (-1)^q v_{-q} \mathbf{e}_q \quad \text{with } q \in \{\pm 1, 0\}. \quad (\text{A2})$$

The vector components (same relations apply also for the \mathbf{e}_q unit vectors) are related to the Cartesian

ones as

$$v_{+1} = -\frac{1}{\sqrt{2}}(v_x + iv_y) \quad v_0 = v_z \quad v_{-1} = \frac{1}{\sqrt{2}}(v_x - iv_y) \quad (\text{A3})$$

$$v_x = \frac{1}{\sqrt{2}}(v_{-1} - v_{+1}) \quad v_z = v_0 \quad v_y = \frac{i}{\sqrt{2}}(v_{-1} + v_{+1}). \quad (\text{A4})$$

Accordingly, the components of the dipole in the SF spherical coordinate system are given in terms of their BF counterparts [73] as

$$\mu_p^{SF} = \sum_{q=-1}^1 D_{pq}^{1*}(\varphi, \theta, \chi) \mu_q^{BF}, \quad \text{with } p \in \{0, \pm 1\}. \quad (\text{A5})$$

Casting also the electric field in spherical form we are able to evaluate

$$\begin{aligned} \mathcal{E}^{SF} \cdot \boldsymbol{\mu}^{SF} &= \sum_{p=-1}^1 (-1)^p \mathcal{E}_{-p}^{SF} \mathbf{e}_p \cdot \sum_{p'=-1}^1 (-1)^{p'} \mu_{-p'}^{SF} \mathbf{e}_{p'} = \sum_{p=-1}^1 (-1)^p \mathcal{E}_{-p}^{SF} \mu_p^{SF} \\ &= \sum_{p=-1}^1 (-1)^p \mathcal{E}_{-p}^{SF} \sum_{q=-1}^1 D_{pq}^{1*}(\varphi, \theta, \chi) \mu_q^{BF} \\ &= \sum_{p=-1}^1 \sum_{q=-1}^1 (-1)^p \mathcal{E}_{-p}^{SF} (-1)^{q-p} D_{-p-q}^1(\varphi, \theta, \chi) \mu_q^{BF} \\ &= \sum_{p=-1}^1 \sum_{q=-1}^1 (-1)^q \mathcal{E}_{-p}^{SF} \mu_q^{BF} D_{-p-q}^1(\varphi, \theta, \chi). \end{aligned} \quad (\text{A6})$$

If one uses linearly polarized laser fields (as in the case of our pump-probe setup, where both pulses are linearly polarized), Eq. (A6) may be simplified to a single sum, retaining the $p = 0$ component for Z -polarized fields $\mathcal{E}_0 \equiv \mathcal{E}_Z$

$$\mathcal{E} \cdot \boldsymbol{\mu} \equiv \mathcal{E}_Z^{SF} \mu_Z^{SF} = \mathcal{E}_Z \sum_{q=-1}^1 (-1)^q \mu_q^{BF} D_{0-q}^1(\varphi, \theta, \chi) \quad (\text{A7})$$

$$\begin{aligned} &= \mathcal{E}_Z [(-1)^{-1} \mu_{-1}^{BF} D_{01}^1(\varphi, \theta, \chi) + (-1)^0 \mu_0^{BF} D_{00}^1(\varphi, \theta, \chi) + (-1)^1 \mu_1^{BF} D_{0-1}^1(\varphi, \theta, \chi)] \\ &= \mathcal{E}_Z \left[-\frac{\mu_x^{BF} - i\mu_y^{BF}}{\sqrt{2}} \frac{\sin \theta}{\sqrt{2}} e^{-i\chi} + \mu_z \cos \theta - \frac{\mu_x^{BF} + i\mu_y^{BF}}{\sqrt{2}} \frac{\sin \theta}{\sqrt{2}} e^{i\chi} \right]. \end{aligned} \quad (\text{A8})$$

In the last line the explicit form of D_{0q}^1 was introduced

$$D_{00}^1(\varphi, \theta, \chi) = \cos \theta, \quad \text{and} \quad D_{0\pm 1}^1(\varphi, \theta, \chi) = \pm \frac{\sin \theta}{\sqrt{2}} e^{\mp i\chi}. \quad (\text{A9})$$

Using the well known identity

$$\begin{aligned} \int_0^{2\pi} d\varphi \int_0^\pi \sin \theta d\theta \int_0^{2\pi} [D_{M_3 \Omega_3}^{J_3}(\varphi, \theta, \chi)]^* D_{M_2 \Omega_2}^{J_2}(\varphi, \theta, \chi) D_{M_1 \Omega_1}^{J_1}(\varphi, \theta, \chi) &= \\ &= \frac{8\pi^2}{2J_3 + 1} C_{J_1 M_1 J_2 M_2}^{J_3 M_3} C_{J_1 \Omega_1 J_2 \Omega_2}^{J_3 \Omega_3} \\ &= 8\pi^2 (-1)^{M_3 + \Omega_3} \begin{pmatrix} J_1 & J_2 & J_3 \\ M_1 & M_2 & -M_3 \end{pmatrix} \begin{pmatrix} J_1 & J_2 & J_3 \\ \Omega_1 & \Omega_2 & -\Omega_3 \end{pmatrix} \end{aligned} \quad (\text{A10})$$

and Eq. (A7) we can develop the expression of matrix elements in the $|JM\Omega\rangle$ basis

$$\begin{aligned} \langle J'M'\Omega' | \boldsymbol{\mathcal{E}} \cdot \boldsymbol{\mu} | JM\Omega \rangle &= \mathcal{E}_Z \sum_{q=-1}^1 (-1)^q \mu_q^{BF} \langle J'M'\Omega' | D_{0-q}^1 | JM\Omega \rangle \\ &= \mathcal{E}_Z \sum_{q=-1}^1 (-1)^q \mu_q^{BF} \left[(-1)^{M'+\Omega'} \sqrt{(2J'+1)(2J+1)} \begin{pmatrix} J & 1 & J' \\ M & 0 & -M' \end{pmatrix} \begin{pmatrix} J & 1 & J' \\ \Omega & -q & -\Omega' \end{pmatrix} \right] \\ &= \mathcal{E}_Z (-1)^{M'+\Omega'} \sqrt{(2J'+1)(2J+1)} \begin{pmatrix} J & 1 & J' \\ M & 0 & -M' \end{pmatrix} \sum_{q=-1}^1 (-1)^q \mu_q^{BF} \begin{pmatrix} J & 1 & J' \\ \Omega & -q & -\Omega' \end{pmatrix} \end{aligned} \quad (\text{A11})$$

The Wigner 3j symbols of the last equation vanish unless the triangular rule of vector addition are satisfied leading to the selection rules

$$M' = M, \quad (\text{A12})$$

$$\Omega' = \Omega - q. \quad (\text{A13})$$

The first one shows that a Z -polarized field leaves the projection of the total angular momenta unchanged. This means that the φ Euler angle is redundant, and can conveniently be fixed to $\varphi = 0$.

Let us recall that all three electronic states of our model are singlet states, meaning that $\mathbf{S} = 0$, therefore $\Omega \equiv \Lambda$. Accordingly, the selection rule (A13) may be rewritten as $\Delta\Lambda = \Lambda' - \Lambda = q$. For this reason, from the expression (A11) of the dipole operator matrix elements, in case of transitions between the Σ states only the $q = 0 - 0 = 0$ term contributes. Note that we would get the same coupling element between Π states, $q = 1 - 1 = 0$. For $\Sigma \leftrightarrow \Pi$ transitions the $\Delta\Lambda_{f \leftarrow i} = \pm 1$ selection

rule applies. As a result, depending on the symmetry of the involved electronic surfaces, only one term of the light-matter coupling expression of Eq. (A8) gives nonzero contribution, namely:

$$\mathcal{E} \cdot \boldsymbol{\mu} = \begin{cases} \mathcal{E}_0 \mu_0^{BF} D_{00}^1(0, \theta, \chi) = \mathcal{E}_Z \mu_z^{BF} \cos \theta & \Sigma \rightarrow \Sigma \text{ (or } \Pi \rightarrow \Pi) \\ -\mathcal{E}_0 \mu_{+1}^{BF} D_{0-1}^1(0, \theta, \chi) = -\mathcal{E}_Z \frac{\mu_x^{BF} + i\mu_y^{BF}}{2} \sin \theta e^{+i\chi} & \Sigma \rightarrow \Pi \\ -\mathcal{E}_0 \mu_{-1}^{BF} D_{01}^1(0, \theta, \chi) = -\mathcal{E}_Z \frac{\mu_x^{BF} - i\mu_y^{BF}}{2} \sin \theta e^{-i\chi} & \Pi \rightarrow \Sigma. \end{cases} \quad (\text{A14})$$

We also have to consider that the Π state is doubly degenerate, with π_{p_x} and π_{p_y} molecular orbitals. Both should be included in the calculations, while the resulting various physical quantities must be averaged over these degenerate states. This would increase the numerical demand of the calculations, since in practice it would mean four electronic states instead of three. To circumvent this inconvenience, we considered them as one, using the below formalism. In case of a $\Sigma \rightarrow \Pi$ transition we can write the corresponding

$$\begin{aligned} \langle \Pi | \mathcal{E} \cdot \boldsymbol{\mu} | \Sigma \rangle &= \langle \Pi_{p_x} | \mathcal{E} \cdot \boldsymbol{\mu} | \Sigma \rangle - i \langle \Pi_{p_y} | \mathcal{E} \cdot \boldsymbol{\mu} | \Sigma \rangle \\ &= -\mathcal{E}_Z \frac{1}{2} \mu_x^{BF} \sin \theta e^{i\chi} - \mathcal{E}_Z \frac{1}{2} \mu_y^{BF} \sin \theta e^{i\chi} \\ &= -\mathcal{E}_Z \mu_{\perp}^{BF} \sin \theta e^{i\chi}. \end{aligned} \quad (\text{A15})$$

In the last equation we used the fact that the x and y components of the dipole moment are equal, and introduced the notation

$$\mu_x^{BF} = \mu_y^{BF} \equiv \mu_{\perp}^{BF}. \quad (\text{A16})$$

Transition in the opposite direction results in a matrix element that is the complex conjugate of (A15), and with $\mu_z^{BF} \equiv \mu_{\parallel}^{BF}$ we arrive to our final expression

$$\langle f | \mathcal{E} \cdot \boldsymbol{\mu} | i \rangle = \begin{cases} \mathcal{E}_Z \mu_{\parallel}^{BF} \cos \theta & \Sigma \rightarrow \Sigma \text{ (or } \Pi \rightarrow \Pi) \\ -\mathcal{E}_Z \mu_{\perp}^{BF} \sin \theta e^{i\chi} & \Sigma \rightarrow \Pi \\ -\mathcal{E}_Z \mu_{\perp}^{BF} \sin \theta e^{-i\chi} & \Pi \rightarrow \Sigma. \end{cases} \quad (\text{A17})$$

[1] A. D. Bandrauk and O. Atabek, J. Phys. Chem. **91**, 6469 (1987).

- [2] E. E. Aubanel and A. D. Bandrauk, *J. Chem. Phys.* **97**, 12620 (1993).
- [3] Y. Arasaki, S. Scheit, and K. Takatsuka, *J. Chem. Phys.* **138**, 161103 (2013).
- [4] S. Scheit, Y. Arasaki, and K. Takatsuka, *J. Chem. Phys.* **140**, 244115 (2014).
- [5] A.K. Tiwari, D. Dey, and N.E. Henriksen, *Phys. Rev. A* **89**, 023417 (2014).
- [6] J. Meisner, M. Vacher, M. J. Bearpark, and M.A. Robb, *J. Chem. Theo. Comp.* **11**, 7 3115 (2015).
- [7] T. Szidarovszky and K. Yamanouchi, *Phys. Rev. A* **94**,6 063405 (2016).
- [8] Y. Arasaki, Y. Mizuno, S. Scheit, and K. Takatsuka, *J. Chem. Phys.***144**, 024106 (2016).
- [9] A. K. Tiwari and N.E. Henriksen, *J. Chem. Phys.* **144**, 014306 (2016).
- [10] A. Tóth, P. Badankó, G. J. Halász, Á. Vibók, and A. Csehi, *Chem. Phys.* **515**, 418-426 (2018).
- [11] S. Zhaopeng, W. Chunyang, Z. Wenkai, and Y. Chuanlu, *J. Chem. Phys.***149**, 224307 (2018).
- [12] P. E. Videla, A. Markmann, and S. Batista, *J. Chem. Theo. Comp.* **14**, 3 1198 (2018).
- [13] F. Bouakline, *J. Phys. Chem. Lett.* **9**, 2271 (2018).
- [14] A. Tóth, A. Csehi, G. J. Halász, and Á. Vibók, *Phys. Rev. A* **99**, 043424 (2019).
- [15] A. Tóth, A. Csehi, G. J. Halász, and Á. Vibók, *Phys. Rev. Res.* **2**, 013338 (2020).
- [16] S. Zhaopeng and L. Yunquan, *Phys. Chem. Chem. Phys.***25**, 17397 (2023).
- [17] Y. Liu, W. Hu, S. Luo, K.J.Yuan, Z. Sun, A.D. Bandrauk, *Phys. Rev. A* **100**, 023404 (2019).
- [18] P.M. Abanador, U. Thumm, *Phys. Rev. A* **102**, 053114 (2020).
- [19] P.M. Abanador, U. Thumm, *Phys. Rev. A* **101**, 043410 (2020).
- [20] Y. R. Liu, Y.Wu, J. G. Wang, O. Vendrell, V. Kimberg, and S. B. Zhang, *Phys. Rev. A* **102**, 033114 (2020).
- [21] Y. R. Liu, Y. Wu, J. G. Wang, O. Vendrell, V. Kimberg, and S. B. Zhang, *Phys. Rev. Res.* **2**, 043348 (2020).
- [22] Y. R. Liu, V. Kimberg, Y.Wu, J. G. Wang, O. Vendrell, and S. B. Zhang, *J. Phys. Chem. Lett.* **12**, 5534 (2021).
- [23] Y. R. Liu, V. Kimberg, Y.Wu, J. G. Wang, O. Vendrell, and S. B. Zhang, *Phys. Rev. Res.***4**, 043001 (2022).
- [24] Y. R. Liu, V. Kimberg, Y.Wu, J. G. Wang, O. Vendrell, and S. B. Zhang, *Phys. Rev. Res.* **4**, 013066 (2022).
- [25] W. Gao, L.L. Ren, R.Q. Liu, Y.C. Han, *Int. J. Quant. Chem.* **121**, 22 e26787 (2021).
- [26] T. Schnappinger, D. Jadoun, M. Gudem, and M. Kowalewski, *Chem. Commun.* **58**, 12763 (2022).
- [27] H. Li, M. Li, A. Petro, E. Tiesinga, and S.Kotochigova, *J. Phys. Chem. A* **127**, 29 (2023).

- [28] X. X. Dong, M. Gong, X. Zhao, Y. R. Liu, Y. Cheng, Y. Wu, J. Wang, J. Chen and S. B. Zhang, *New J. Phys.* **26**, 013050 (2024).
- [29] O. Umarov, A. Csehi, P. BadankÅł, G. J. Halász, and Á. Vibók, *Phys. Chem. Chem. Phys.* **26**,7211 (2024).
- [30] E. M. Liane, M. Simmermacher, and A. Kirrander, *J. Phys. B: At. Mol. Opt. Phys.* **57**, 145602 (2024).
- [31] Z. Sun, Y. Liu, *J. Phys. Chem. A* **128**, 25 (2024).
- [32] W. Gao, L. L. Ren, S. H. Jing, and Y. C. Han, *Phys. Scr.* **99**, 085415 (2024).
- [33] J. Liu, J. Li, D. Zhang, and D. Ding, *Chin. Phys. B* **34**, 103101 (2025).
- [34] P. Recio, J. CachÅłn, A. Zanchet, S. M. Poullain, and L. Bañares, *J. Chem. Phys.* **158**, 234304 (2023).
- [35] J. CachÅłn, P. Recio, A. Zanchet, S. M. Poullain, and L. Bañares, *J. Chem. Phys.* **159**, 064302 (2023).
- [36] M. Saab, M. Sala, B. Lasorne, F. Gatti, and S. GuÅłřin, *J. Chem. Phys.* **141**, 134114 (2014).
- [37] C. Sanz-Sanz, G. W. Richings, and G. A. Worth, *Faraday Discussions*, **153**, 275 (2011).
- [38] H. Choi, W. J. Son, S. Shin, B. Y. Chang, and I. R. Sola, *J. Chem. Phys.* **128**, 104315 (2008).
- [39] B. Y. Chang, H. Choi, S. Shin, S. Lee, and I. R. Sola, *J. Mod. Opt.* **56**, 811 (2009).
- [40] V. Tagliamonti, P. SÁndor, A. Zhao, T. Rozgonyi, P. Marquetand and T. Weinacht, *Phys. Rev. A* **93**, 051401 (2016).
- [41] M. Assmann, T. Weinacht, and S. Matsika, *J. Chem. Phys.* **144**,034301 (2016).
- [42] H. V. S. Lam, S. Yarlagadda, Anbu Venkatachalam, et al., *Phys. Rev. A* **102**, 049119 (2020).
- [43] C. Avanesian, Y. Wang, and D. R. Yarkony, *J. Phys. Chem. Lett.* **15**,9905 (2024).
- [44] M. Born and R. Oppenheimer, *Ann. Phys.* **84**, 457 (1927).
- [45] H. KÅłppel, W. Domcke, and L. S. Cederbaum, *Adv. Chem. Phys.* **57**, 59 (1984).
- [46] D. R. Yarkony, *Rev. Mod. Phys.* **68**, 985 (1996).
- [47] G. A. Worth and L. S. Cederbaum, *Annu. Rev. Phys. Chem.* **55**, 127 (2004).
- [48] W. Domcke, D. R. Yarkony, and H. KÅłppel, *Conical Intersections: Electronic Structure, Dynamics and Spectroscopy*; World Scientific: Singapore; (2004).
- [49] M. Baer, *Beyond Born Oppenheimer: Electronic Non-Adiabatic Coupling Terms and Conical Intersections*, Wiley: Hoboken, NJ, 2006.
- [50] N. Moiseyev, M. Sindelka, and L. S. Cederbaum, *J. Phys. B* **41**, 221001 (2008).
- [51] G. J. Halász, M. Sindelka, N. Moiseyev, L. S. Cederbaum, and Á. Vibók, *J. Phys. Chem. A* **116**, 2636 (2012).
- [52] G. J. Halász, Á. Vibók, N. Moiseyev, and L. S. Cederbaum, *Phys. Rev. A* **88**, 043413 (2013).

- [53] G. J. Halász, A. Csehi, Á. Vibók, and L.S. Cederbaum, *J. Phys. Chem. A* **118**, 11908 (2014).
- [54] G. J. Halász, Á. Vibók, and L. S. Cederbaum, *J. Phys. Chem. Lett.* **6**, 348 (2015).
- [55] A. Csehi, G. J. Halász, L. S. Cederbaum, and Á. Vibók, *J. Chem. Phys.* **143**, 0143305 (2015).
- [56] A. Csehi, G. J. Halász, L. S. Cederbaum, and Á. Vibók, *J. Chem. Phys.* **144**, 8 (2016).
- [57] A. Csehi, G. J. Halász, L. S. Cederbaum, and Á. Vibók, *Faraday Discuss.* **194**, 479 (2016).
- [58] A. Csehi, G. J. Halász, L. S. Cederbaum, and Á. Vibók, *J. Phys. Chem. Lett.* **8**, 1624 (2017).
- [59] T. Szidarovszky, G. J. Halász, A. G. Császár, L. S. Cederbaum, and Á. Vibók, *J. Phys. Chem. Lett.* **9**, 2239 (2018).
- [60] C. C. Shu, K. J. Yuan, D. Dong, I. R. Petersen, and A. D. Bandrauk, *J. Phys. Chem. Lett.* **8**, 1 (2017).
- [61] A. Natan, M. R. Ware, V. S. Prabhudesai, U. Lev, B. D. Bruner, O. Heber, and P. H. Bucksbaum, *Phys. Rev. Lett.* **116**, 143004 (2016).
- [62] M. Křžbel, M. Spanner, Z. Dube, A. Yu. Naumov, S. Chelkowski, A. D. Bandrauk, M. J. J. Vrakking, P. B. Corkum, D. M. Villeneuve, and A. Staudte, *Nat. Com.* **11**, 2596 (2020).
- [63] J. Kim, H. Tao, J. L. White, V. S. Petrovič, T. J. Martinez, and P. H. Bucksbaum, *J. Phys. Chem. A* **116**, 2758 (2012).
- [64] M. E. Corrales, J. González-Vázquez, G. Balerdi, I. R. Solá, R. de Nalda, and L. Bañares, *Nature Chem.* **6**, 785 (2014).
- [65] C. Fábri, B. Lasorne, G. J. Halász, L. S. Cederbaum, and Á. Vibók, *J. Phys. Chem. Lett.* **11**, 5324 (2020).
- [66] A. Bhattacharjee and K. R. Dastidar, *Phys. Rev. A* **65**, 022701 (2002).
- [67] M. Aymar, J. Deiglmayr, and O. Dulieu, *Can. J. Phys.* **87**, 543 (2009).
- [68] A. Bhattacharjee and K. R. Dastidar, *J. Phys. B: At. Mol. Opt. Phys.* **36**, 4467 (2003).
- [69] Q. Guo, J.-W. Hu, J. Qi, J. Yu, and Y.-C. Han, *Laser Physics*, **32**, 045701 (2022).
- [70] H. J. Werner, P. J. Knowles, G. Knizia, F. R. Manby, M. Schřtz, et al. MOLPRO, version 2015.1, a package of ab initio programs. (2015); see <http://www.molpro.net> (accessed May 11, 2016).
- [71] E. S. Sachs, J. Hinze, and N. H. Sabelli, *J. Chem. Phys.* **62**, 3367 (1975).
- [72] E. S. Sachs, J. Hinze, and N. H. Sabelli, *J. Chem. Phys.* **62**, 3384 (1975).
- [73] R. N. Zare, *Angular Momentum: Understanding Spatial Aspects in Chemistry and Physics* (John Wiley & Sons, New York, 1988).
- [74] H. D. Meyer, U. Manthe, and L. S. Cederbaum, *Chem. Phys. Lett.* **165**, 73 (1999).
- [75] G. A. Worth, et. al. The MCTDH package, version 8.6, University of Heidelberg, Germany;

<http://mctdh.uni-hd.de/> 2023.

- [76] H. D. Meyer, F. Gatti and G. A. Worth, *Multidimensional Quantum Dynamics: MCTDH Theory and Applications* (Weinheim: Wiley-VCH) 2009.
- [77] Z. Király, O. Umarov, Cs. Fábri, G. J. Halász, A. Tóth, and Á. Vibók Raw data and figure generating scripts (Zenodo, Geneva, 2025) <https://doi.org/10.5281/zenodo.18958928>